PHYSICAL REVIEW D **84,** 024036 (2011)

Falloff of the Weyl scalars in binary black hole spacetimes

Ian Hinder,* Barry Wardell,† and Eloisa Bentivegna‡

Max-Planck-Institut für Gravitationsphysik, Albert-Einstein-Institut, Am Mühlenberg 1, D-14476 Golm, Germany

(Received 6 May 2011; published 19 July 2011)

The peeling theorem of general relativity predicts that the Weyl curvature scalars Ψ_n ($n = 0, \ldots, 4$), when constructed from a suitable null tetrad in an asymptotically flat spacetime, fall off asymptotically as r^{n-5} along outgoing radial null geodesics. This leads to the interpretation of Ψ_4 as outgoing gravitational radiation at large distances from the source. We have performed numerical simulations in full general relativity of a binary black hole inspiral and merger, and have computed the Weyl scalars in the standard tetrad used in numerical relativity. In contrast with previous results [Phys. Rev. D **80**, 121502 (2009).], we observe that all the Weyl scalars fall off according to the predictions of the theorem.

DOI: 10.1103/PhysRevD.84.024036 PACS numbers: 04.25.dg, 04.20.Ha, 04.30.Db

I. INTRODUCTION

Spacetimes containing multiple black holes (BHs) are perhaps the most studied class of nonperturbative, low-symmetry vacuum solutions of Einstein's equations and have already opened the path to tests of the generality of a number of fundamental theorems and conjectures in general relativity.

Studies of multiple-BH systems have addressed the behavior of trapped surfaces and tubes [1–7] and event horizons [8–14] during the dynamical many-body phase. The asymptotic properties (such as the radial falloff of the Weyl scalars) of binary-black-hole (BBH) spacetimes have been investigated [15], and the algebraic character of BBH spacetimes has been studied [16,17]. A program to include conformal infinity in the numerical domain has been carried out [18–20], and properties of higher-dimensional BBH systems have been described [21–23]. Several interesting directions remain to be explored in the context of multiple-BH evolutions [24–29].

It seems fair to state that three-dimensional numerical evolutions of Einstein's equations are now leading to compelling and useful results for gravitational fields in nontrivial configurations. While this class of numerical relativity (NR) studies may appear somewhat removed from the field of gravitational-wave astrophysics, the clarification of fundamental issues has a direct impact there. For instance, the interpretation of Ψ_4 as the outgoing component of gravitational radiation relies entirely on the applicability of the peeling theorem.

In this work, we follow up the study carried out in [15], where the radial falloff of the Weyl scalars was measured in a BBH spacetime and compared with the results expected from the peeling theorem. We use the same evolution code and the same definitions of the Weyl scalars. However, we use an independent and open analysis framework provided by the Einstein Toolkit initiative [30] for computing the scalars,[1] and we analyze their falloff properties using a more direct approach. Our results indicate that all of the Ψ_n fall off at the expected rates, suggesting that the usual techniques used for wave extraction in NR simulations are sufficient for recovering the results of the peeling theorem. We present our method in Sec. II and the results we obtain in Sec. III. We conclude with a discussion in Sec. IV. Throughout this paper, we use a spacelike signature $(-, +, +, +)$ and a system of units in which $c = G = 1$.

II. METHODOLOGY

A. The Weyl scalars and the peeling theorem

The work of Sachs [32], Newman and Penrose [33] illustrates how the information encoded in the traceless part of the Riemann curvature tensor, the Weyl tensor C_{abcd}, can be completely expressed as a set of five complex numbers usually referred to as the *Weyl scalars*:

$$\Psi_0 = C_{abcd}\ell^a m^b \ell^c m^d \tag{1a}$$

$$\Psi_1 = C_{abcd}\ell^a n^b \ell^c m^d \tag{1b}$$

$$\Psi_2 = C_{abcd}\ell^a m^b \bar{m}^c n^d \tag{1c}$$

$$\Psi_3 = C_{abcd}\ell^a n^b \bar{m}^c n^d \tag{1d}$$

$$\Psi_4 = C_{abcd}n^a \bar{m}^b n^c \bar{m}^d \tag{1e}$$

where $(n^a, \ell^a, m^a, \bar{m}^a)$ is a tetrad of two real and two complex null vectors satisfying $n_a n^a = 0$, $\ell_a \ell^a = 0$, $n_a \ell^a = -1$, $m_a m^a = 0$ and $m_a \bar{m}^a = 1$.

Handling the curvature in this notation has a number of benefits: from the geometric standpoint, there is immediate

*ian.hinder@aei.mpg.de
†barry.wardell@aei.mpg.de
‡eloisa.bentivegna@aei.mpg.de

[1]The unexpected results pointed out in [15] for the peeling properties of Ψ_0 and Ψ_1 were affected by errors in the original analysis implementation which have subsequently been corrected. As an aside, we note that ensuring correctness is a subtle and involved part of developing complex scientific applications [31]. We believe that collaborative development and the use of open-source software is one of the simplest and most effective ways to ensure code correctness.

insight to be gained as the five Ψ_n are simply the spin-frame components of the Weyl spinor Ψ_{ABCD}. Thus if the spin-frame has some physical relevance (e.g. is oriented along principal null directions), then the Ψ_n can be identified as specific (radiative vs Coulomb, transverse vs longitudinal) components of the gravitational field [34]. From the practical side, the five complex quantities above simplify the analysis of the asymptotic properties of the Riemann tensor (see, e.g., [33,35]). In particular, the work of Newman and Penrose shows how these scalars fall off along outgoing radial null geodesics in a neighborhood of future null infinity, $\mathcal{J}^+$, as:

$$\Psi_n \sim r^{n-5}. \tag{2}$$

(For the parallel result on $\mathcal{J}^-$, see e.g. [36].) The usual assumptions of the Penrose conformal construction are assumed, namely, the existence of a spacetime conformally related to the physical one by $g_{ab}^{\text{unphys}} = \Omega^2 g_{ab}^{\text{phys}}$, with $\Omega = 0$ at $\mathcal{J}^+$, the falloff of the corresponding Weyl tensor at least as $C_{abcd}^{\text{unphys}} \sim \Omega$, also at $\mathcal{J}^+$, and the alignment of n^a and ℓ^a with the ingoing and outgoing null directions, respectively (accomplished, for instance, by setting $n_a = \Omega_{;a}$). In the above, $r \equiv \Omega^{-1}$ can be used, at least in a neighborhood of $\mathcal{J}^+$, as the affine parameter on the null geodesic. In typical asymptotically-flat spacetimes, this can be identified with a radial coordinate, as long as the Weyl tensor satisfies the above falloff condition when expressed in terms of it. This result, known as the peeling theorem, is a convenient tool for evaluating integrals at $\mathcal{J}^+$ and allows one to identify Ψ_4 with the outgoing gravitational-wave degrees of freedom since, for one, it is the only component with an associated flux at $\mathcal{J}^+$ that is not identically zero:

$$\int_{\mathcal{J}^+} |\Psi_n|^2 dS \neq 0 \Rightarrow n = 4. \tag{3}$$

Notice that, while this result is rather robust and valid in a large class of tetrad (or spinor) frames, it does rely on a suitable choice of r. A question that was recently raised in [15] is to what extent the peeling theorem can be directly applied to the Weyl scalars usually calculated in NR simulations of BBH systems, where a dynamically-evolving gauge can obscure the character of the coordinates, from which the tetrad is usually constructed. This question is closely related to similar investigations carried out in the NR literature, such as what conditions should be imposed on the tetrad frame in order to retain the interpretation of Ψ_4 as outgoing gravitational waves [28], or how many principal null directions exist in post-merger black hole remnants [16,17].

In this work, we investigate the extent to which the falloff rates predicted by the peeling theorem apply to BBH spacetimes as usually computed in NR. There are two aspects to this question: whether a numerical spacetime satisfies the theorem's physical requirements (the falloff condition for the Weyl tensor), and whether the dynamical coordinates are compatible with the assumptions.

B. Tetrad

In numerical simulations, where the domain does not typically include $\mathcal{J}^+$ (the notable exception being simulations using characteristic extraction [18,19]), the tetrad $(n^a, \ell^a, m^a, \bar{m}^a)$ is usually chosen according to the following straightforward prescription [37]. First, one defines the spatial vectors ϕ^a, r^a and θ^a via their spatial components:

$$\phi^i = [-y, x, 0], \tag{4a}$$
$$r^i = [x, y, z], \tag{4b}$$
$$\theta^i = \sqrt{\gamma}\epsilon^i_{jk}\phi^j r^k. \tag{4c}$$

where γ is the determinant of the spatial metric. One then uses Gram-Schmidt orthonormalization to produce the orthonormal triad

$$\begin{aligned} e^a_\phi &= \frac{\phi^a}{\| \phi \|}, \\ e^a_r &= \frac{r^a - P_{e_\phi} r^a}{\| r - P_{e_\phi} r \|}, \\ e^a_\theta &= \frac{\theta^a - P_{e_\phi} r^a - P_{e_r} \theta^a}{\| \theta - P_{e_\phi} r - P_{e_r} \theta \|}, \end{aligned} \tag{5}$$

where $P_x y^a \equiv (x_b y^b) x^a$ is the projection of a vector y^a along a unit vector x^a, $\| v \| = \sqrt{v_a v^a}$, and indices are raised and lowered with the spatial metric. Finally, one complements this triad with the unit hypersurface normal u^a and constructs the null tetrad as

$$\begin{aligned} l^a &= \frac{1}{\sqrt{2}}(u^a + e^a_r), & n^a &= \frac{1}{\sqrt{2}}(u^a - e^a_r), \\ m^a &= \frac{1}{\sqrt{2}}(e^a_\theta + i e^a_\phi), & \bar{m}^a &= \frac{1}{\sqrt{2}}(e^a_\theta - i e^a_\phi). \end{aligned} \tag{6}$$

The normalization in Eq. (6) follows a common convention [37] used in NR and differs from the conventions usually used in other fields. This can lead to constant-factor differences between expressions computed using this convention and those appearing elsewhere in the literature.

Unfortunately, due to the degeneracy in the azimuthal coordinate, ϕ, this tetrad is not defined on the z axis. We overcome this problem by making the particular choice $\phi = \pi$, so that $\phi^i = [1, 0, 0]$ and the tetrad is once again well defined (note, however, that the tetrad—and hence the Weyl scalars—remain discontinuous across the z axis).

C. Approximate null geodesics

We wish to investigate the extent to which the Weyl scalars as computed using the tetrad in Sec. II B obey the peeling property along some suitably defined curves in a BBH spacetime. For the peeling theorem to apply, the

curves should be outgoing radial null geodesics; this is because the Weyl scalars vary not only in advanced time (according to the peeling theorem), but also in retarded time. A failure to use exact outgoing null geodesics as the curves along which to measure the falloff results in a mixing of these two dependencies, leading to an error in the measured falloff. This error may be significant or not, depending on the extent of the deviation from exact geodesics. It would be possible to calculate the exact null geodesics in a numerical spacetime, but this is not typically done, and we have not done so here as it turns out to be unnecessary for confirming the applicability of the peeling theorem to BBH spacetimes. Instead, we compute a series of *approximate null geodesics*, defined as curves in the x–t coordinate plane along which local maxima of $|\Psi_4|$ propagate. In the geometric optics approximation, these curves will be null geodesics.

By restricting the approximate null geodesics to the x–t plane, we are assuming that the outgoing null geodesics which are asymptotically radial have a negligible angular coordinate dependence in the region in which we study them. This is a reasonable expectation given that in Kerr, with spin parameter equal to that of the final post-merger black hole ($J/M^2 \approx 0.68$), the angular deviation of an asymptotically radial outgoing null geodesic between $r = 30M$ and $r = 1000M$ is only 10^{-3} radians.

One may expect that an even simpler approximation would suffice and make the assumption that the null geodesics correspond approximately to those of the Schwarzschild spacetime in Schwarzschild coordinates. In this case the null geodesics are given by $r_* = t + \text{const}$, where $r_* = r + 2M\ln(r/2M - 1)$ is the tortoise coordinate. At large radius, this is not an unreasonable expectation. However, close to the black holes this approximation becomes increasingly poor. Unfortunately, Ψ_0 and Ψ_1 fall off sufficiently fast that they drop below the level of numerical error before the region $r \approx 100M$ where the Schwarzschild approximation becomes reliable, so this approximation is unsuitable for measuring the falloff of these scalars.

D. Falloff measurement

Given the Weyl scalars computed using the coordinate tetrad (6) and an approximate null geodesic $r = \lambda(t)$, described in the previous section, we consider the falloff of the scalars with the coordinate radius r. In order to determine a representative value for the falloff rate, we choose an interval $r \in [r_{\min}, r_{\max}]$ and perform a linear least-squares fit of

$$\log|\Psi_n(t, \lambda(t))| = -p \log r + \text{const} \tag{7}$$

to determine p.

The appropriate choice of the interval is influenced by two factors. First, since the peeling theorem predicts only the asymptotic behavior of the scalars, we desire a fitting interval at as large a radius as possible so that the subleading terms are negligible. Secondly, we find that Ψ_0 and Ψ_1 are dominated by numerical error (visible as spatial oscillations at the maximum grid frequency and comparable in magnitude to the signal) at large r and large t, and that this limits the maximum radius at which we can fit.

E. Numerical implementation

Our numerical BBH solutions were obtained using the LLAMA code [38] to solve Einstein's equations in the BSSN [39–41] formalism with the moving puncture method [42,43] using eighth-order finite differencing. The computational infrastructure is based on the CACTUS framework [44,45] and the CARPET [46–48] adaptive mesh-refinement driver, and implements a system of multiple grid patches with data exchanged via interpolation [38]. This multipatch technique allowed us to use a spherical outer grid with constant angular resolution to best match the resolution requirements of radially outgoing waves, leading to an outer boundary at very large radius at only modest computational cost. This enabled us to measure the Weyl scalars accurately at a large radius, where they are closer to their asymptotic form.

We studied an equal-mass binary system with an initial separation of $6M$ and both black holes initially nonspinning. The configuration studied in [15] had a larger initial separation and hence a longer gravitational-wave signal. However, the length of the wave signal should not be important for measuring the falloff, so we ran a shorter simulation for computational efficiency. We computed standard Bowen-York [49,50] initial data with parameters given in Table I using the TWOPUNCTURES [51] code.

In our simulations, calculation of the Weyl scalars was performed by WEYLSCAL4, a component of the open Einstein Toolkit [52]. We have adapted WEYLSCAL4 to utilize the LLAMA multipatch framework and have performed careful testing against analytic results for the I invariant [37] in Kerr. We have also cross-checked WEYLSCAL4 against PSIKADELIA [53], another code which computes the Weyl scalars. Since this code was developed independently, the agreement is strong evidence that the codes are both correct.

We performed simulations at two different grid spacings (the detailed grid structures used in our runs are listed in Table II) to assess the effect of the numerical discretization

TABLE I. Initial data parameters for the equal-mass, nonspinning configuration studied. M is the sum of the initial irreducible masses of the black holes, and $m_{\rm h}$ is the irreducible mass of each BH. $m_{\rm b}/M$, D/M, p_r/M and p_t/M are the bare mass, separation, radial and tangential momenta used in the Bowen-York initial data prescription.

$m_{\rm h}/M$	$m_{\rm b}/M$	D/M	p_r/M	p_t/M
0.5	0.476 534 633 02	6	−0.005 867 766	0.138 357 448

TABLE II. Numerical grid parameters of the BBH simulations studied. Both multipatch (M) and Cartesian (C) simulations were run at two resolutions (a and b). In all cases h_0 is the grid spacing on the coarsest Cartesian grid. In cases where an angular grid is used this is also equal to the radial grid spacing in the angular patches. $N_{\rm ang}$ is the number of cells in the angular directions in the angular patches. $R_{\rm in}$ and $R_{\rm out}$ are the inner and outer radii of the angular patches. $N_{\rm lev}$ is the number of refinement levels (including the coarsest) on the Cartesian grid, and $r_{\rm l}$ indicates that a cubical refinement box of side $2r_{\rm l}$ is centered on the BH on level "l," with level 0 being the coarsest.

Run	h_0/M	$N_{\rm ang}$	$R_{\rm in}/M$	$R_{\rm out}/M$	$N_{\rm lev}$	$r_{\rm l}/M$
Ma	0.69	28	39.77	2697.6	6	12,6,3,1.5,0.6
Mb	0.60	32	39.6	2697.6	6	12,6,3,1.5,0.6
Ca	0.69	-	-	200.0	6	12,6,3,1.5,0.6
Cb	0.60	-	-	200.0	6	12,6,3,1.5,0.6

on the solution. Owing to high frequency numerical reflections from the interpatch and refinement boundaries, we found it necessary to modify the grid structure when computing the falloff of Ψ_0 and Ψ_1 which, being the fastest decaying and lowest in amplitude, are the most affected by these reflections. In this case, we eliminated the angular grid patches entirely and used a purely Cartesian domain with an outer boundary causally disconnected from the region in which we could resolve these Weyl scalars. We found that the errors coming from refinement boundaries visible in Ψ_0 could be reduced significantly by switching the mesh-refinement algorithm used from the standard Berger-Oliger [54] scheme to the tapered grids scheme of [55]. This has the effect of eliminating the errors caused by time interpolation at the mesh-refinement boundaries. (The tapered grid scheme when used with eighth-order finite differencing typically introduces a very high computational cost on the refined levels, but in our case the coarse level has so many grid points that this cost increase was not significant.)

III. RESULTS

We now present the results of applying the fitting methods to the simulations described in Sec. II E.

We consider the falloff of the Weyl scalars along curves λ_i in spacetime which correspond to the peaks $i = 1 \ldots 7$ of $|\Psi_4|$ shown in Fig. 1. This is a plot of $|\Psi_4|$ along the x axis at fixed coordinate time $t = 720M$. Note that for this configuration, all of the Weyl scalars are either purely real or purely imaginary along the x axis.

Figure 2, plotted on a log-log scale, shows the falloff of the Weyl scalars along the curve λ_1 in the x–t plane corresponding to the peak labeled 1 in Fig. 1 as a function of the radial coordinate r. The peeling theorem predicts that the Weyl scalars Ψ_n fall off asymptotically as r^{n-5} corresponding to straight lines in this figure. The solid curves represent the numerical data and the dashed lines represent the best fit straight line (the line for the expected falloff is not shown, but in each case is visually very similar to the line obtained from the fit). We see that to a very good approximation, each scalar exhibits a power-law decay as predicted by the peeling theorem.

For each scalar, we choose an appropriate fitting interval (see Sec. II D) and compute the falloff rate by performing a least-squares fit in this interval. For Ψ_2, Ψ_3 and Ψ_4, the scalars are well resolved at all radii in our simulations (we stopped the simulations when the signal reached $r = 1000M$). We therefore choose a fitting interval $r \in [100M, 1000M]$ in this case. For Ψ_0 and Ψ_1, the scalars are dominated by numerical error beyond $r \approx 60M$, as we observed when comparing the results at different numerical resolutions. We therefore choose a fitting interval $r \in [30M, 45M]$ for these. The fitting intervals are indicated on the plot as black vertical lines on each curve.

We have performed this analysis for each of the 7 curves and for each resolution. For Ψ_0 and Ψ_1, only λ_1 and λ_2 yield meaningful measurements of the falloff rate; there is too much finite differencing error in the solution on λ_3–λ_7 to compute a falloff rate.

The shaded regions in Fig. 2 (visible only for Ψ_0 and Ψ_1) represent an indication of the error due to finite

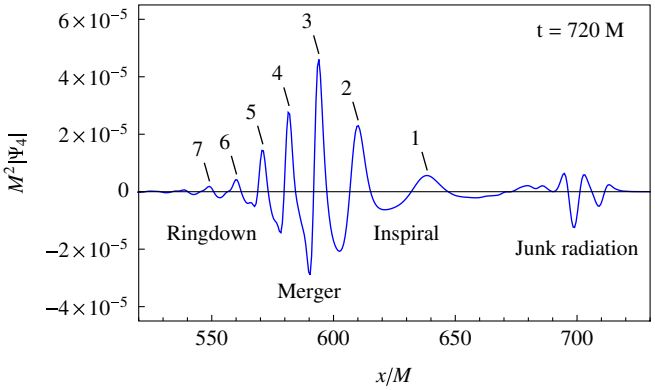

FIG. 1 (color online). $|\Psi_4|$ on the x axis. Note that since there is no multipolar decomposition, this looks different to the waveform plots usually shown in papers. Specifically, the junk radiation is on the right and the wave propagates to the right. The numbered labels indicate the peaks corresponding to the approximate null geodesics λ_i that we compute.

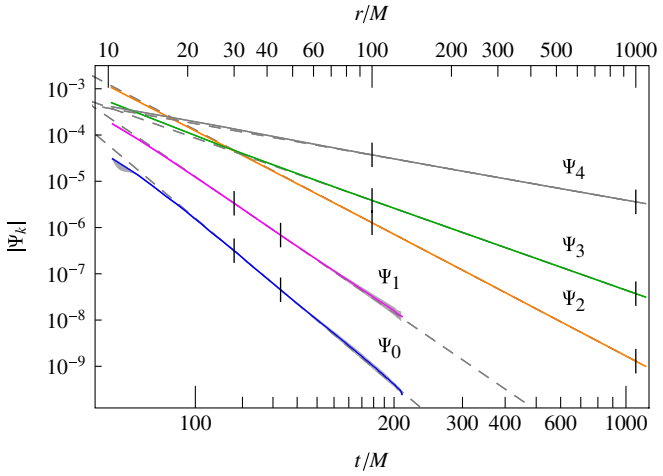

FIG. 2 (color online). The falloff of the Weyl scalars along the approximate null geodesic λ_1 corresponding to the first inspiral peak of $|\Psi_4|$ on the x axis. The falloff rates obtained from fitting in the intervals indicated by vertical black lines are indicated in Table III.

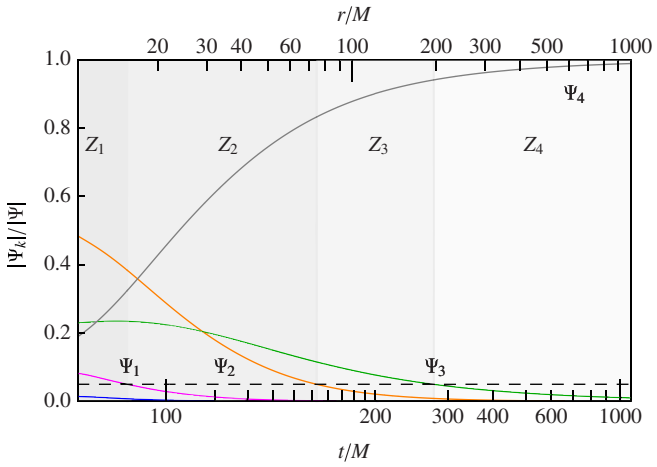

FIG. 3 (color online). The fractional contribution of each Ψ_n (measured along λ_1) to the *total curvature*, which we define as $|\Psi| = \sum_{n=0}^{4} |\Psi_n|$. The zones Z_n are the regions in which Ψ_k, for $k \geq n$, give a contribution of more than 5% to Ψ. Beyond $r \gtrsim 200M$, Ψ_4 dominates and may be reliably used as a measure of gravitational radiation. Note that Z_0 does not appear as Ψ_0 is already below 5% at $r = 10M$, where we can first start tracking the peak in $|\Psi_4|$.

differencing, computed using the two different resolutions and assuming eighth-order convergence of the error. This should be taken as indicative only, as the convergence rate obtained can vary between 3 and 8 at finite resolution, corresponding to the different sources of numerical error in the simulation.

Table III shows the falloff rates for each scalar along λ_1 as well as the rate quoted in [15] and the rate expected from the peeling theorem. The finite differencing error in the last digit is indicated in parentheses and again should be taken as only a coarse estimate. The rates obtained from λ_2–λ_7 (not shown) differ by less than 2% from those obtained for λ_1 (only the curves on which the rates are sufficiently well resolved are included). Our measured rates are within 4% of the values expected from the peeling theorem.

By studying the peeling properties of each of the Weyl scalars we may gain insight into where Ψ_4 may be used as a reasonable measure of the gravitational-wave signal.

TABLE III. Falloff rates for the Weyl scalars, including the rate expected from the peeling theorem, the rate obtained in [15], and the rate measured from our simulations for the approximate null geodesic λ_1. The error in the last digit indicated in parentheses is a coarse estimate of the finite differencing error in the falloff rate.

	Falloff rate p		
Ψ	Expected	Ref. [15]	Measured
0	5	2.00	4.8(4)
1	4	2.48	3.91(7)
2	3	2.99	2.993 07(6)
3	2	1.99	2.0135(6)
4	1	0.99	1.013 33(7)

This is closely related to the identification of the regions referred to as *near zone*, *transition zones* and *radiation zone* in [33] (note that these are not the same zones referred to in [56]). We illustrate this visually (for the curve for λ_1) in Fig. 3, where we plot the relative contribution from each of the Weyl scalars to the *total curvature*, which we define as $|\Psi| = \sum_{n=0}^{4} |\Psi_n|$. Each shaded region Z_n indicates the region in which all the Ψ_k with $k \geq n$ give a contribution of more than 5% to the total curvature (notice that this also comes with a change in the algebraic properties of the spacetime, since the principal null directions "peel apart" as each Ψ_n becomes important with decreasing r). In other words, as the source is approached from $r = \infty$, Z_n is the region in which Ψ_n starts to make a significant contribution. In the case of our BBH simulations, we find that Ψ_4 constitutes more than 95% of $|\Psi|$ in the region $r \gtrsim 200M$. We observe that Ψ_3, Ψ_2 and Ψ_1 begin to contribute >5% to the curvature at $r = 200M$, $75M$ and $15M$, respectively. Note that the values of r depend on the curve λ_i along which the falloff is measured and on the choice of cut-off percentage. For example, the regions Z_n start at lower radii for the subsequent peaks resulting in Z_4 beginning at $r \approx 100M$ rather than $200M$. This may be understood from the fact that these peaks closer to the merger have stronger gravitational-wave content with the result that Ψ_4 is comparatively larger.

IV. DISCUSSION

We have performed a 3-orbit BBH simulation and measured the falloff of the Weyl scalars, obtaining results in agreement with the peeling theorem to within 4%.

There are many approximations introduced in converting the precise assumptions of the theorem into practical numerical calculations. For example, in this work we approximated null geodesics by tracking the location of peaks in $|\Psi_4|$ along the x axis. This neglects any angular component in the null geodesics and also assumes that the peaks propagate along null geodesics. Furthermore, we used a coordinate tetrad which we assume satisfies the assumptions of the peeling theorem. The fact that we found agreement with the predictions gives strong evidence in support of the approaches and approximations typically used in NR simulations.

As in [15], accurate falloff rates were easily extracted for Ψ_2, Ψ_3 and Ψ_4, where the finite differencing error was negligible and the deviation from the expected rate was almost certainly due to computing the falloff at a finite radius, where subleading terms are nonzero.

However, due to the presence of a large amount of numerical noise, Ψ_0 and Ψ_1 proved much more difficult to analyze. This is not surprising given that the spacetime we are considering—a BBH inspiral—has a strong outgoing radiation component (Ψ_4 and Ψ_3) and Coulomb-type potential (Ψ_2) and only weak incoming radiation (Ψ_1 and Ψ_0). Nevertheless, by minimizing errors coming from interpatch and mesh-refinement boundaries, we were able to compute Ψ_0 and Ψ_1 in a sufficiently large region to extract falloff rates within 4% of the expected values.

As discussed in Sec. III and Fig. 2, the rapid falloff of Ψ_0 means that it drops to a level where it is strongly affected by numerical noise for $r \gtrsim 60M$. Furthermore, for $r \gtrsim 100M$ it reaches a point where it is orders of magnitude below the other Ψ_n and its contribution to the curvature is negligible. This indicates that any approximations based on the vanishing of Ψ_0—for example "freezing-Ψ_0" boundary conditions [57,58]—are robust at these large radii.

We have also shown a representative example of the radial *zones* in which each of the Weyl scalars begins to contribute to the total curvature. In the case of our BBH simulations, we found that Ψ_4 constituted more than 95% of $|\Psi|$ in the region $r \gtrsim 200M$. The identification of the zones in Fig. 3 is valid for the equal-mass, nonspinning BBH configuration we have studied here. While we expect this to be representative of other configurations—possibly involving spins and unequal masses—it is likely that the exact locations of the peeling regions will be different.

The use of Ψ_4 to compute gravitational waveforms from NR BBH solutions is based on the assumption that the peeling theorem can be applied. Although it is reasonable to expect that this is true, this work provides reassuring confirmation that this is indeed the case.

ACKNOWLEDGMENTS

It is a pleasure to thank A. Helfer, D. Pollney, C. Reisswig, and E. Schnetter for reading a draft of this manuscript and providing helpful comments and suggestions. We also thank D. Pollney, C. Reisswig, E. Schnetter, N. Dorband, and P. Diener for providing the LLAMA/CTGAMMA multipatch evolution code used in this work, as well as all the authors of CACTUS, CARPET and the Einstein Toolkit for providing the open and optimized infrastructure on which our simulations are based. The computations were performed on the Datura cluster at the AEI and on the Teragrid network (allocation TG-MCA02N014). E. B. acknowledges support from a Marie Curie International Reintegration Grant under Agreement No. PIRG05-GA-2009-249290. This work was supported in part by the DFG under Grant SFB/Transregio 7 "Gravitational-Wave Astronomy."

[1] E. Schnetter, F. Herrmann, and D. Pollney, Phys. Rev. D **71**, 044033 (2005).
[2] M. Campanelli, C. O. Lousto, and Y. Zlochower, Phys. Rev. D **74**, 084023 (2006).
[3] M. Campanelli, C. O. Lousto, Y. Zlochower, B. Krishnan, and D. Merritt, Phys. Rev. D **75**, 064030 (2007).
[4] E. Schnetter, B. Krishnan, and F. Beyer, Phys. Rev. D **74**, 024028 (2006).
[5] B. Szilágyi, D. Pollney, L. Rezzolla, J. Thornburg, and J. Winicour, Classical Quantum Gravity **24**, S275 (2007).
[6] M. Jasiulek, Classical Quantum Gravity **26**, 245008 (2009).
[7] R. Owen, Phys. Rev. D **80**, 084012 (2009).
[8] R. Matzner *et al.*, Science **270**, 941 (1995).
[9] J. Massó, E. Seidel, W.-M. Suen, and P. Walker, Phys. Rev. D **59**, 064015 (1999).
[10] S. A. Caveny, M. Anderson, and R. A. Matzner, Phys. Rev. D **68**, 104009 (2003).
[11] P. Diener, Classical Quantum Gravity **20**, 4901 (2003).
[12] M. Alcubierre *et al.*, Phys. Rev. D **72**, 044004 (2005).
[13] M. I. Cohen, H. P. Pfeier, and M. A. Scheel, Classical Quantum Gravity **26**, 035005 (2009).
[14] M. Ponce, C. Lousto, and Y. Zlochower, arXiv:1008.2761.
[15] D. Pollney, C. Reisswig, N. Dorband, E. Schnetter, and P. Diener, Phys. Rev. D **80**, 121502 (2009).
[16] M. Campanelli, C. O. Lousto, and Y. Zlochower, Phys. Rev. D **79**, 084012 (2009).
[17] R. Owen, Phys. Rev. D **81**, 124042 (2010).
[18] C. Reisswig, N. Bishop, D. Pollney, and B. Szilágyi, Classical Quantum Gravity **27**, 075014 (2010).
[19] C. Reisswig, N. Bishop, D. Pollney, and B. Szilágyi, Phys. Rev. Lett. **103**, 221101 (2009).

[20] M. C. Babiuc, B. Szilagyi, J. Winicour, and Y. Zlochower, arXiv:1011.4223.
[21] M. Zilhao *et al.*, Phys. Rev. D **81**, 084052 (2010).
[22] H. Witek *et al.*, Phys. Rev. D **82**, 104014 (2010).
[23] H. Witek *et al.*, Phys. Rev. D **83**, 044017 (2011).
[24] J. Karkowski and E. Malec, Acta Phys. Pol. B **36**, 59 (2005).
[25] J. L. Jaramillo, N. Vasset, and M. Ansorg, arXiv:0712.1741.
[26] S. Dain and O. E. Ortiz, Phys. Rev. D **80**, 024045 (2009).
[27] M. Mars, Classical Quantum Gravity **26**, 193001 (2009).
[28] L. Lehner and O. M. Moreschi, Phys. Rev. D **76**, 124040 (2007).
[29] E. Gallo, L. Lehner, and O. M. Moreschi, Classical Quantum Gravity **26**, 048002 (2009).
[30] ''Einstein Toolkit: Open software for relativistic astrophysics," http://einsteintoolkit.org/.
[31] R. G. Sargent, in *Proceedings of the 31st Conference on Winter Simulation*, Simulation—a bridge to the future Vol. 1, WSC '99 (ACM, New York, 1999), p. 39.
[32] R. K. Sachs, Proc. R. Soc. A **264**, 309 (1961).
[33] E. Newman and R. Penrose, J. Math. Phys. (N.Y.) **3**, 566 (1962); **4**, 998(E) (1963).
[34] P. Szekeres, J. Math. Phys. (N.Y.) **6**, 1387 (1965).
[35] E. T. Newman and T. Unti, J. Math. Phys. (N.Y.) **3**, 891 (1962).
[36] M. Walker and C. Will, Phys. Rev. D **19**, 3495 (1979).
[37] J. G. Baker, M. Campanelli, and C. O. Lousto, Phys. Rev. D **65**, 044001 (2002).
[38] D. Pollney, C. Reisswig, E. Schnetter, N. Dorband, and P. Diener, Phys. Rev. D **83**, 044045 (2011).
[39] T. Nakamura, K. Oohara, and Y. Kojima, Prog. Theor. Phys. Suppl. **90**, 1 (1987).
[40] M. Shibata and T. Nakamura, Phys. Rev. D **52**, 5428 (1995).
[41] T. W. Baumgarte and S. L. Shapiro, Phys. Rev. D **59**, 024007 (1998).
[42] J. G. Baker, J. Centrella, D.-I. Choi, M. Koppitz, and J. van Meter, Phys. Rev. Lett. **96**, 111102 (2006).
[43] M. Campanelli, C. Lousto, P. Marronetti, and Y. Zlochower, Phys. Rev. Lett. **96**, 111101 (2006).
[44] T. Goodale, G. Allen, G. Lanfermann, J. Masso, T. Radke, E. Seidel, and J. Shalf, in *Vector and Parallel High Performance Computing in Computational Sciences–VECPAR 2002*, Lecture Notes in Computer Science Vol. 2565, edited by J. M. L. M. Palma, J. Dongarra, V. Hernandez, and A A. Sousa (Springer, Berlin, 2003), p. 15.
[45] ''Cactus computational toolkit," http://www. cactuscode .org.
[46] E. Schnetter, S. H. Hawley, and I. Hawke, Classical Quantum Gravity **21**, 1465 (2004).
[47] E. Schnetter, P. Diener, E. N. Dorband, and M. Tiglio, Classical Quantum Gravity **23**, S553 (2006).
[48] ''Carpet: Adaptive Mesh Refinement for the Cactus Framework," http://www.carpetcode.org/.
[49] J. M. Bowen and J. W. York, Phys. Rev. D **21**, 2047 (1980).
[50] S. Brandt and B. Brügmann, Phys. Rev. Lett. **78**, 3606 (1997).
[51] M. Ansorg, B. Brügmann, and W. Tichy, Phys. Rev. D **70**, 064011 (2004).
[52] ''Einstein toolkit," http://www.einsteintoolkit.org.
[53] The PSIKADELIA code was written by Steven Brandt (sbrandt@cct.lsu.edu) and Paul Walker.
[54] M. J. Berger and J. Oliger, J. Comput. Phys. **53**, 484 (1984).
[55] L. Lehner, S. L. Liebling, and O. Reula, Classical Quantum Gravity **23**, S421 (2006).
[56] K. Thorne, Rev. Mod. Phys. **52**, 299 (1980).
[57] L. E. Kidder, L. Lindblom, M. A. Scheel, L. T. Buchman, and H. P. Pfeiffer, Phys. Rev. D **71**, 064020 (2005).
[58] L. T. Buchman and O. C. Sarbach, Classical Quantum Gravity **24**, S307 (2007).